



The synergistic effect between Ni sites and Ni-Fe alloy sites on hydrodeoxygenation of lignin-derived phenols

Qiao Han^a, Mooneez Ur Rehman^a, Junhu Wang^b, Alexandre Rykov^b, Oliver Y. Gutiérrez^c, Yujun Zhao^{a,*}, Shengping Wang^a, Xinbin Ma^a, Johannes A. Lercher^{c,d}

^a Key Laboratory for Green Chemical Technology of Ministry of Education, Collaborative Innovation Center of Chemical Science and Engineering, School of Chemical Engineering and Technology, Tianjin University, Tianjin, 300072, China

^b Mössbauer Effect Data Center, Dalian Institute of Chemical Physics, Chinese Academy of Sciences, Dalian, 116023, China

^c Institute for Integrated Catalysis, Pacific Northwest National Laboratory, Richland, WA, 99352, United States

^d Department of Chemistry and Catalysis Research Center, TU München, Garching, 85748, Germany

ARTICLE INFO

Keywords:

Phenol
Hydrodeoxygenation
Cyclohexane
Ni-Fe alloy
Kinetics

ABSTRACT

The catalytic hydrodeoxygenation (HDO) of lignin-derived phenolic compounds is a critical step in the upgrading of bio-oil. Here, bimetallic Ni-Fe nanoparticles supported on mesoporous carbon spheres (MCSs) were fabricated and applied in HDO of phenol. In comparison with monometallic Ni and Fe catalysts, the bimetallic Ni-Fe catalyst exhibited better performance for phenol HDO due to the formation of Ni-Fe alloy phase identified by X-ray powder diffraction (XRD) and Mössbauer spectroscopy techniques. Among several explored ratios, the catalysts with Ni/Fe ratio of 3/1 presented the highest cyclohexane yield. The reaction occurred in two consecutive steps: the hydrogenation of phenol to cyclohexanol and the further hydrogenolysis of cyclohexanol to cyclohexane. Kinetic studies showed that the hydrogenolysis of cyclohexanol controlled the overall reaction rate of phenol HDO due to the lower reaction rate of this step. Indeed, the turnover frequency (TOF) values of cyclohexanol normalized by surface metallic Ni sites exhibited a linear correlation with Ni-Fe alloy sites. The alloying of iron in the bimetallic Ni-Fe catalysts significantly enhanced the adsorption strength of cyclohexanol, which is the reason of the high activity of the Ni-Fe alloy particles. Thus, Fe-containing sites adsorb the hydroxyl species while Ni sites perform the H₂ activation, their synergistic effect plays a key role in phenol HDO process.

1. Introduction

With the gradual shrink of the petroleum reserves, bio-oils have been regarded as an important alternative for the depleting hydrocarbon sources [1–3]. Lignocellulosic bio-oils, typically produced by fast pyrolysis process, have been regarded as an important feed for the production of renewable chemical energy. However, the high oxygen content in lignin-derived bio-oils results in poor properties in comparison with fossil fuels [4,5], such as high acidity, poor stability and low heating value [6–8], making it an inappropriate fuel [9]. Therefore, it is particularly important to upgrade the bio-oils by removing their oxygen by means of catalytic hydrodeoxygenation (HDO) [10–12].

In terms of the active phases, HDO catalysts can be classified into the following categories [13]: (1) metal sulfides; (2) noble metals; (3) metal carbides, nitrides, and phosphides; and (4) base metal. The application of metal sulfide catalysts, such as MoS₂ [14], CoMoS₂ [15], and NiMoS₂ [16,17] was relatively early. Although showing satisfactory

activity, they are quickly deactivated in the presence of water [2]. In addition, the re-sulfurization process can not only complicate the procedure [18] but also pollutes the environment. Supported Pt, Pd, and Ru catalysts [19–23] are excellent hydrogenation catalysts, but they usually require to be combined with acidic sites to enhance their deoxygenation activity [19–21,24] due to their weak oxyphilicity [25]. Metal carbide, nitride, and phosphide catalysts [26–29] have received much more attentions in recent years due to their catalytic behavior that resembles that of noble metal catalysts [13,30]. However, these materials face the same problem as metal sulfides in terms of deactivation and regeneration. For the past few years, base metal catalysts have been rapidly developed for HDO reactions, which has been encouraged by their low price in comparison with noble catalysts. Ni [31] and Co [32] catalysts showed prominent hydrogenation activity, and Fe [33], W [34] and Mo [35] catalysts exhibited remarkable oxygen affinity.

Jin et al. [36] found high activity of supported Ni for saturation of

* Corresponding author.

E-mail address: yujunzhao@tju.edu.cn (Y. Zhao).

<https://doi.org/10.1016/j.apcatb.2019.04.065>

Received 2 January 2019; Received in revised form 14 April 2019; Accepted 19 April 2019

Available online 22 April 2019

0926-3373/ © 2019 Elsevier B.V. All rights reserved.

aromatic rings during anisole HDO. The excellent hydrogenation ability of Ni has been further shown by Mortensen et al. [9] in the phenol HDO with high yield of cyclohexanol. However, monometallic Ni catalysts exhibit low selectivity to oxygen-free products, such as cyclohexane derivatives. The use of bimetallic formulations could help overcoming this limitation [37–40]. Fe, which is more oxyphilic than Ni, has been found to facilitate the hydrogenation of C=O and the hydrogenolysis of C–O in furfural conversion [37] as well as the deoxygenation of methyl laurate [38]. Fang et al. [40] reported that bimetallic Ni-Fe catalysts afforded high conversion of guaiacol and significantly enhanced the selectivity to phenol or cyclohexane by tuning Ni/Fe ratio. However, the role of iron in the bimetallic Ni-Fe formulation has not yet been clarified, and the mechanism for C–O bonds cleavage on these catalysts is still under debate.

In the present work, a suite of monometallic Ni, Fe, and bimetallic Ni-Fe nanoparticles supported on mesoporous carbon spheres (MCSs) catalysts were prepared. MCSs provide a large specific surface area while being catalytically inert under reaction conditions, which allows to study the metallic phase alone. The structural changes of bimetallic Ni-Fe catalysts with varying Ni/Fe ratios were analyzed by X-ray powder diffraction (XRD), transmission electron microscopy, (TEM), H₂ temperature programmed reduction (H₂-TPR), and Mössbauer spectroscopy techniques. Thermogravimetric (TG) analysis was used to measure the adsorption of cyclohexanol and determine the concentration of sites amounts for cyclohexanol adsorption. Kinetics of individual steps for phenol HDO were investigated to reveal the rate-determining step. The catalytic performance for HDO of both phenol and cyclohexanol was evaluated, and the synergistic effect between Ni and Ni-Fe alloy active sites for phenol HDO was discussed.

2. Experimental

2.1. Chemicals

Paraffin liquid (> 99.0%), sorbitan monooleate (Span 80) (C₂₄H₄₄O₆, CP), resorcinol (C₆H₆O₂, AR), formaldehyde solution (37 wt.% in water) were purchased from Shanghai Macklin Biochemical Co., Ltd. And colloidal silica sol (30 wt.%, 10–20 nm) was provided by Qingdao Yuminyuan Silica gel Reagent Factory. Nickel nitrate (Ni(NO₃)₂·6H₂O, AR), iron nitrate (Fe(NO₃)₃·9H₂O, AR), phenol (C₆H₆O, ≥ 99.5%), cyclohexanol (C₆H₁₂O, > 99.0%), catechol (C₆H₆O₂, > 99.0%), guaiacol (C₇H₈O₂, > 99.0%), p-cresol (C₇H₈O, > 99.0%), eugenol (C₁₀H₁₂O₂, > 99.0%) and n-decane (C₁₀H₂₂, > 99.0%) were obtained from Shanghai Aladdin Bio-Chem Technology Co., Ltd. n-dodecane (C₁₂H₂₆, > 98.0%) was purchased from Meryer (Shanghai) Chemical Technology Co., Ltd.

2.2. Catalyst preparation

The MCSs supports were fabricated through the method described in detail elsewhere [41]. The bimetallic Ni-Fe catalysts were prepared by a co-impregnation method. Typically, the MCSs supports were impregnated with nickel nitrate and iron nitrate which were dissolved in 50% ethanol solution maintaining a total metal mass loading of 10 wt.% or 20 wt.%, and the Ni/Fe ratio was accordingly adjusted. After that, the thick liquid was dried at ambient temperature for 12 h and 50 °C for another 12 h, and then calcined at 400 °C for 6 h with a heating rate of 3 °C min^{−1} in Ar atmosphere. Prior to catalytic activity evaluation, the catalysts were reduced in H₂ at a flow rate of 60 mL·min^{−1} at 400 °C for 4 h with a heating rate of 2 °C min^{−1}. After cooling to room temperature, the reduced catalysts were passivated for 1 h using 1% O₂-Ar to prevent oxidation. The bimetallic catalysts were labeled as mNi_x-Fe_y/MCSs, where *m*, *x* and *y* represent the total metal mass loading, the atomic ratios of Ni and Fe, respectively.

2.3. Catalyst characterization

Static nitrogen physical adsorption-desorption at −196 °C method was employed to obtained specific surface area, pore volume and average pore diameter using a Micromeritics Tristar II 3000 analyzer instrument. The passivated samples were degassed at 100 °C for 1 h and at 300 °C for another 3 h in vacuum prior to analysis.

The actual loading of nickel and iron in the catalysts were detected by inductively coupled plasma optical emission spectrometry (ICP-OES) (Vista-MPX, Varian).

X-ray powder diffraction (XRD) patterns of the catalysts were recorded at room temperature by a Rigaku C/MAX-2500 diffractometer equipped with a Cu Kα radiation source (γ = 1.5406 Å). The patterns were obtained from 30° to 80°.

Scanning electron microscopy (SEM) micrographs were taken on a S-4800 instrument. The samples were ultrasonically dispersed in ethanol for 30 min.

Transmission electron microscopy (TEM) and high-resolution TEM (HRTEM) and STEM energy dispersive spectroscopy (STEM-EDS) micrographs were obtained on a JEM-2100F instrument operated at 200 kV. The pretreatment method was the same as the SEM. For particle size statistics, about 200–300 nanoparticles were counted in 5 separate images for each catalyst sample.

H₂ temperature programmed reduction (H₂-TPR) was gotten on a Micromeritics Autochem II 2910 equipped with a thermal conductivity detector (TCD). In each experiment, 30 mg of calcinated samples were placed into a U-type quartz tube and dried in Ar at 200 °C for 2 h. After cooling to ambient temperature, the samples were then heated in 10% H₂/Ar to 800 °C with the heating rate of 10 °C min^{−1}.

⁵⁷Fe Mössbauer spectroscopy at the room temperature was used to characterize the atomic structure of iron species by using a Topologic 500 A spectrometer and a proportional counter. The γ-ray radioactive source of ⁵⁷Co (Rh) moved in a constant acceleration mode.

H₂ chemisorption were carried out on a Micromeritics Autochem II 2920 equipped with a TCD. In each experiment, 50 mg of calcined samples were first reduced at 400 °C in presence of H₂ for 2 h followed by purging with Ar at 400 °C for 1 h to remove physisorbed molecules. After cooling to 30 °C, 10% H₂/Ar pulses were passed through the U-type quartz tube until the area of consecutive pulses was constant.

Cyclohexanol adsorption and desorption were studied via thermogravimetric (TG) and derivative thermogravimetric (DTG) analysis on a NETZSCH STA 449F5 instrument. Background collection was implemented as follows. About 6 mg of MCSs support was placed in the crucible, followed by heating to 250 °C under Ar atmosphere. Then the saturated vapor of cyclohexanol at 50 °C was carried by Ar at a flow rate of 100 mL·min^{−1} through the sample cell, and both the flow rate of purge gas and protective gas were 20 mL·min^{−1}. After the adsorption proceeded for 1 h, the lines were purged with Ar at 250 °C for 10 min, and then the sample was heated to 400 °C with a rate of 5 °C min^{−1} and held at 400 °C for 1 h for desorption analysis. Bimetallic Ni-Fe catalysts were tested under the same conditions as those of the background collection.

2.4. Catalytic performance

Typically, 50 mg of passivated catalyst was introduced into a Parr autoclave (100 ml of volume) containing 0.5 g of phenol or other oxygenated compound and 24.5 g of n-dodecane. Then, the autoclave was purged five times with 0.2 MPa of Ar. When the target temperature was reached, the autoclave was pressurized with 5 MPa of H₂, which was the starting point of the reaction. The stirring rate was kept at 800 rpm. After reaction, the autoclave was cooled to ambient temperature. Toluene was then added into the system to dissolve unreacted phenol and n-decane was added as internal standard. The filtered liquid products were analyzed by using gas chromatograph (Agilent Micro GC 4890) equipped with a flame ionization detector and an HP-INNOWAX

Table 1
Physicochemical properties of the MCSs support and 10Ni-Fe/MCSs with varying Ni/Fe ratios.

Samples	$S_{\text{BET}}^a/\text{m}^2\text{g}^{-1}$	$V_t^a/\text{cm}^3\text{g}^{-1}$	$D_{\text{pore}}^a/\text{nm}$	Total metal loading ^b /wt. %	Ni/Fe ratio ^b	Crystallite size ^c /nm	Particle size $\pm \delta^d$ /nm	H ₂ uptake ^e	
								$\mu\text{mol g}_{\text{cat}}^{-1}$	$\mu\text{mol g}_{\text{Ni}}^{-1}$
MCSs	770	2.3	13.7	–	–	–	–	–	–
10Ni/MCSs	727	2.1	13.0	9.6	∞	4.8	7.4 ± 1.8	21.1	221
10Ni ₅ -Fe ₁ /MCSs	711	2.0	13.9	9.4	4.94	4.6	7.2 ± 1.2	15.4	195
10Ni ₃ -Fe ₁ /MCSs	728	2.0	13.4	9.3	2.81	4.5	6.8 ± 1.0	7.9	113
10Ni ₁ -Fe ₁ /MCSs	729	2.1	13.5	9.7	0.91	2.9	6.1 ± 1.2	2.4	51
10Ni ₁ -Fe ₃ /MCSs	718	1.9	12.9	9.3	0.32	2.5	6.6 ± 1.2	0.6	27
10Fe/MCSs	715	2.0	13.9	9.4	0	–	7.9 ± 1.2	–	–

^a Determined by N₂ isotherm adsorption-desorption.

^b Determined by ICP-OES.

^c Calculated by the Scherrer equation using Ni or Fe₁Ni₃ (111) lattice plane.

^d Determined via TEM, and δ is standard deviation.

^e Determined by H₂ chemisorption.

capillary column (Hewlett-Packard Company, 30 m \times 0.32 mm \times 0.50 μm). The conversion of reactants, the selectivity to each product were defined as follows:

$$\text{Conversion} = \frac{(\text{moles of reactant})_{\text{in}} - (\text{moles of reactant})_{\text{out}}}{(\text{moles of reactant})_{\text{in}}} \times 100\% \quad (1)$$

$$\text{Selectivity} = \frac{\text{moles of product i}}{\sum \text{moles of products}} \times 100\% \quad (2)$$

3. Results and discussion

3.1. Structural characterization

The physicochemical properties of the MCSs support and bimetallic 10Ni-Fe/MCSs are listed in Table 1. The specific surface areas of the MCSs support determined through the Brunauer–Emmett–Teller (BET) method is 770 m² g^{−1}, and the surface areas of the catalysts present a slight decrease in comparison with the support. This suggests that metallic nanoparticles could be dispersed in the pores of MCSs. All catalysts have nearly the similar pore volume and pore size, which are 1.9–2.1 cm³ g^{−1} and 12.9–13.9 nm, respectively. The ICP-OES data shows that all the bimetallic 10Ni-Fe catalysts have total metal loadings closing to 10 wt. %, and Ni/Fe ratio is very close to the expected value.

The XRD patterns of the MCSs support and reduced bimetallic 10Ni-Fe/MCSs catalysts with varying Ni/Fe ratios are presented in Fig. 1. The broad diffraction peak at $2\theta = 44.3^\circ$ are assigned to the MCSs support. For the monometallic 10Fe/MCSs, the diffraction peaks at $2\theta = 35.5^\circ$,

43.0° and 62.7° correspond to Fe₃O₄ (JCPDS No. 00-001-1111). The monometallic 10Ni/MCSs shows diffraction peaks at $2\theta = 44.4^\circ$, 51.6° and 76.1° , which are ascribed to the Ni (111), (200) and (220) lattice planes (JCPDS No. 00-001-1258), respectively. These diffraction peaks shifted to lower angles with increasing iron content, which indicates the formation of Ni-Fe alloy for bimetallic 10Ni-Fe catalysts [37–40,42]. The diffraction peaks observed at $2\theta = 43.9^\circ$, 51.2° and 75.4° are ascribed to the Fe₁Ni₃ alloy phase (JCPDS No. 00-012-0736). The crystallite size of monometallic Ni and bimetallic Ni-Fe catalysts, calculated by Scherrer equation using Ni or Fe₁Ni₃ (111) lattice planes are summarized in Table 1. The crystallite size decreases with increasing iron content suggesting that iron is likely to promote the dispersion of nickel [38,40].

SEM and TEM images of the MCSs support are displayed in Fig. 2 (A) and (B). The nanoparticle size distribution of as-reduced bimetallic catalysts is illustrated in Fig. S1 and the mean particle sizes are summarized in Table 1. As shown in Fig. 2 (A) and (B), the MCSs support possesses a well-defined spherical morphology. With the decrement of Ni/Fe ratio, the average particle size shows a trend of first decreasing and then increasing. And the nanoparticles size is the smallest when Ni/Fe ratio is 1/1 (Table 1). It is noteworthy that the introduction of a moderate Fe content could promote the dispersion of Ni, whereas an excessive amount of Fe may lead to the agglomeration of the metallic particles. It might originate from the contribution of the interactions between nickel and iron, known as the geometric and stabilizing effect [37,42,43] in bimetallic catalysts [44–46]. HRTEM images, STEM-EDS linear scanning and mapping of as-reduced 10Ni₃-Fe₁/MCSs catalyst

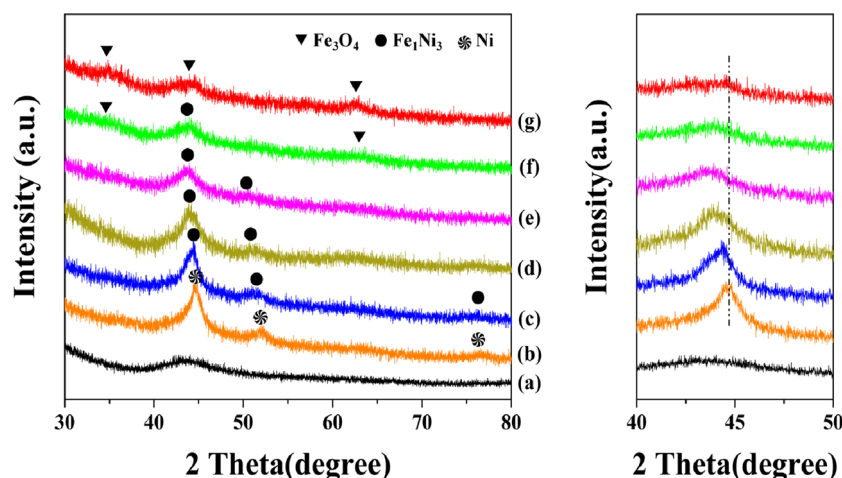


Fig. 1. XRD patterns of the MCSs support and bimetallic 10Ni-Fe/MCSs with varying Ni/Fe ratios: (a) MCSs, (b) 10Ni/MCSs, (c) 10Ni₅-Fe₁/MCSs, (d) 10Ni₃-Fe₁/MCSs, (e) 10Ni₁-Fe₁/MCSs, (f) 10Ni₁-Fe₃/MCSs and (g) 10Fe/MCSs.

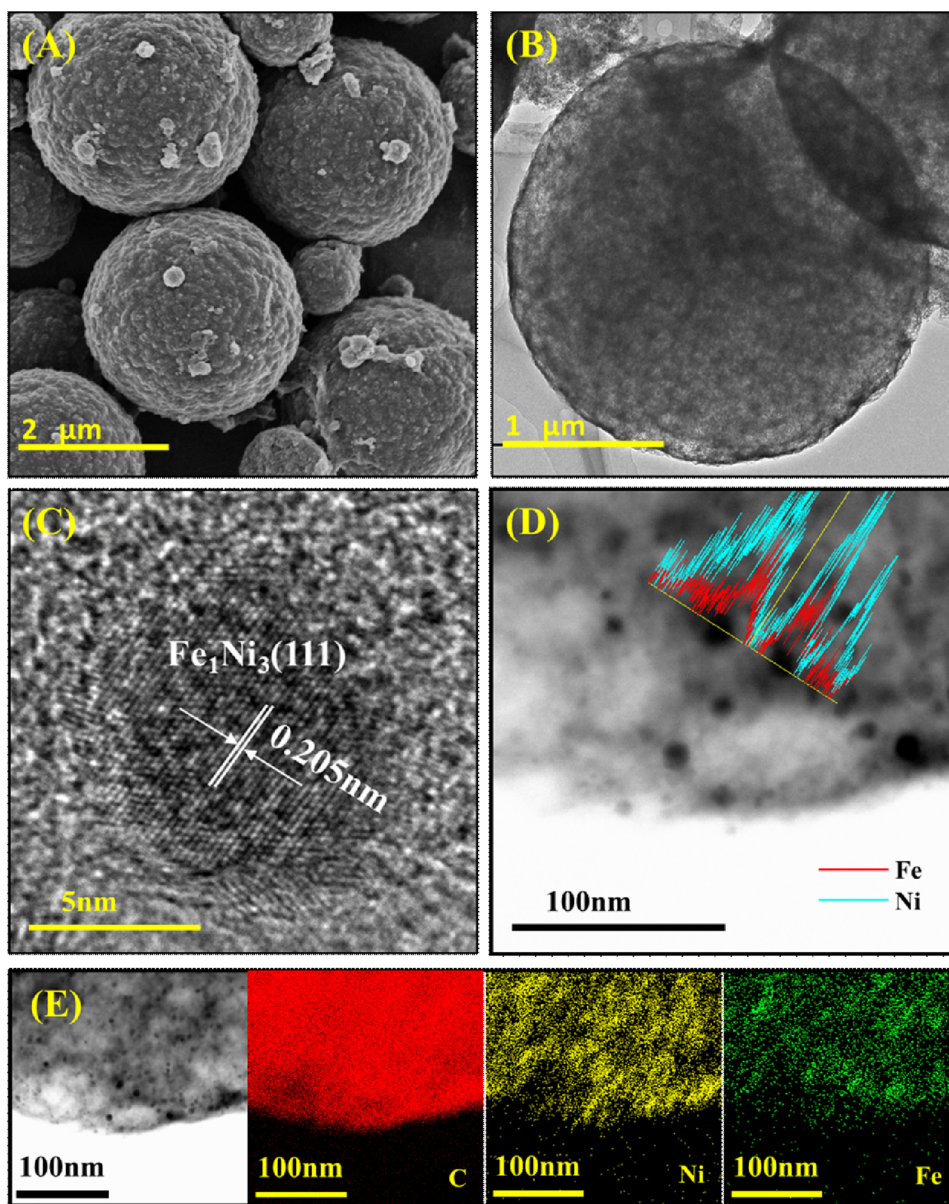


Fig. 2. (A) SEM and (B) TEM images of the MCSs support, (C) HRTEM image, (D) STEM-EDS linear scanning and (E) mapping of reduced 10Ni₃-Fe₁/MCSs.

are shown in Fig. 2 (C)–(E). As shown in Fig. 2 (C), the lattice fringes scanned from the representative nanoparticle have a 0.205 nm distance, which is in line to the (111) lattice plane of Fe₁Ni₃ alloy (JCPDS No. 00-012-0736) [42,47–49]. The formation of Ni-Fe alloy is further confirmed by STEM-EDS linear scanning and mapping results, which is showed in Fig. 2 (D) and (E). The signal intensities of Ni and Fe species along the line are consistent with the nominal compositions. Moreover, there are uniform dispersion of Ni and Fe elements over the MCSs. In short, highly dispersed bimetallic Ni-Fe nanoparticles supported on MCSs were successfully synthesized with the formation of Ni-Fe alloy.

H₂-TPR was employed to illustrate the interaction between Ni and Fe. In the reference experiment shown in Fig. 3(a), a low-intensity broad reduction peak ranging from 500 °C to 800 °C was observed in the TPR characterization of bare MCSs, which is attributed to the reduction of oxygen-containing functional groups on the MCSs supports (14% oxygen content measured by XPS) to form CO₂ or CO as well as methanation of carbon [36,50,51]. As shown in Fig. 3, the reduction profile for the monometallic 10Ni/MCSs precursor displays one broad hydrogen consumption peak with the maximum temperature at ~460 °C, ascribed to the reduction of NiO to Ni. This reduction temperature is

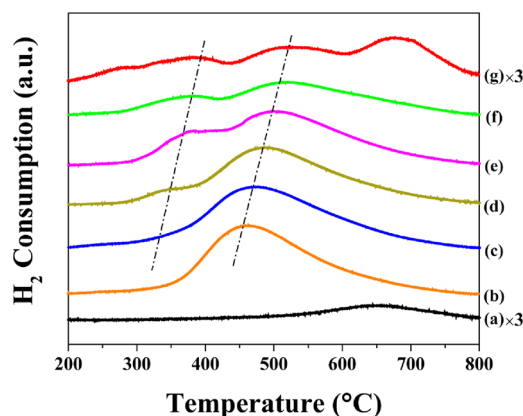


Fig. 3. H₂-TPR profiles of calcined bimetallic 10Ni-Fe/MCSs with varying Ni/Fe ratios: (a) MCSs, (b) 10Ni/MCSs, (c) 10Ni₅-Fe₁/MCSs, (d) 10Ni₃-Fe₁/MCSs, (e) 10Ni₁-Fe₁/MCSs, (f) 10Ni₁-Fe₃/MCSs and (g) 10Fe/MCSs.

much higher than those reported of Ni catalyst with carbon supports [52,53]. This shift to high temperature is attributed to the interaction between metal species and the oxygen-containing functional groups on the surface of the support [36]. For the monometallic 10Fe/MCSs precursor, there were three broad H_2 consumption peaks. The peaks at 385 °C, 525 °C and 677 °C were assigned to the reduction of $\alpha\text{-Fe}_2\text{O}_3$ to Fe_3O_4 , Fe_3O_4 to FeO and FeO to $\alpha\text{-Fe}$, respectively [54–56], indicating that iron oxide cannot be completely reduced under 400 °C. For the bimetallic 10Ni-Fe/MCSs catalysts, their precursors have only two hydrogen appreciable consumption peaks, implying the simultaneous reduction of nickel and iron bimetallic oxide followed by the formation of Ni-Fe alloy. A gradual shift to lower reduction temperature and increase of H_2 consumption result from the addition of Ni also point to the interaction between nickel and iron [37,49,57]. In other words, the efficient dissociation of H_2 by Ni accelerates the reduction of iron oxide [40,48].

The H_2 chemisorption method was applied to determine the amounts of active sites for hydrogen adsorption on the catalysts. As listed in Table 1, H_2 uptake of monometallic 10Ni/MCSs is $21.1 \mu\text{mol g}_{\text{cat}}^{-1}$. With decreasing of Ni content in the bimetallic catalysts, the H_2 uptake decreases gradually. For the monometallic 10Fe/MCSs catalyst, there is no apparent H_2 chemisorption. As is well known, Fe has a much lower activity in H_2 activation than Ni does [38]. Hence, to explain the influence of iron on nickel, H_2 uptake is normalized by the mass of nickel. As displayed in Table 1, H_2 uptake of 10Ni/MCSs catalyst is $221 \mu\text{mol g}_{\text{Ni}}^{-1}$ and it decreases with the increase of iron content. These results indicate that the addition of Fe inhibits H_2 adsorption on Ni sites. The XPS (X-ray photoelectron spectroscopy) result (Table S1) shows that the average Ni/Fe atomic ratio (Ni/Fe = 1.50) on the catalyst surface is much lower than the bulk ratio (Ni/Fe = 2.81 on basis of the ICP-OES result). It indicates that iron species could be rich on the surface of Ni nanoparticles [38]. The surface segregation of iron species on the bimetallic Ni-Fe catalyst system has been already reported by some other work [49,58,59].

Mössbauer spectra is the most suitable characterization for iron, thus it was used for determining the Fe species in these bimetallic Ni-Fe catalysts. However, it was difficult to accurately characterize the highly dispersed Fe-containing catalysts with only 10% of total metal loading. Therefore, the catalysts with 20 wt.% of total metal loading were prepared to study the Fe species in the catalysts. As shown in Fig. 4 and Table 2, 20Fe/MCSs shows a quadrupole doublet and a magnetic sextet, indicating it has two kinds of iron species. The doublet with an IS of $0.3\text{--}0.46 \text{ mm s}^{-1}$ and a QS of $0.72\text{--}0.96 \text{ mm s}^{-1}$ is typically attributed to Fe^{3+} species [60]. A sextet with H_0 of 32.6 T is assigned to Fe^0 [61]. While for bimetallic Ni-Fe catalysts, all the spectra have a quadrupole doublet, a singlet and a magnetic sextet, indicating that 20Ni₅-Fe₁/MCSs, 20Ni₃-Fe₁/MCSs and 20Ni₁-Fe₁/MCSs catalysts have three distinct iron species. Besides Fe^{3+} species, the presence of singlet with an IS of $0.19\text{--}0.21 \text{ mm s}^{-1}$ and magnetic sextet with H_0 of 28.7–30.1 T in the Mössbauer spectra strongly proves the formation of Ni-Fe alloy (fcc) and Ni-Fe alloy (bcc) phase, respectively [62].

3.2. HDO of phenol on 10Ni-Fe/MCSs

The performance of the 10Ni-Fe/MCSs with varying Ni/Fe ratios in HDO of phenol is listed in Table 3. The monometallic 10Ni/MCSs catalyst presents a high conversion of more than 99% but poor cyclohexane selectivity, resulting in a cyclohexane yield of only 8.7%. As previously reported, Ni is often used in hydrogenation of aromatic rings due to its high-efficiency of hydrogen adsorption and dissociation [63–65]. The monometallic 10Fe/MCSs catalyst shows much lower activity (conversion = 6.4%) than 10Ni/MCSs. When the Ni/Fe ratio is greater than 1/1, without exception, the conversion of phenol is higher than 99%, indicating that the amount of Ni active sites is enough for phenol hydrogenation to cyclohexanol, regardless of the decreased Ni content and the inhibiting effect of Fe on Ni species in H_2 chemisorption

and dissociation. But when Ni/Fe ratio is 1/3, the conversion of phenol drops to 82.3%, which is ascribed to substantial decrease of Ni active site concentration. The formation of cyclohexanol from phenol and the cyclohexanol to cyclohexane is a cascade reaction [2]. Thus, in the situation of near-complete conversion of phenol, the high selectivity of cyclohexane means a high activity for conversion of cyclohexanol. The most important effect of Ni/Fe ratio on HDO of phenol is the product distribution. Compared to monometallic 10Ni/MCSs, once a small amount of iron is added to the catalysts, the yield of cyclohexane is increased from 8.7% to 30.5%. However, the higher Fe content does not mean the higher yield of cyclohexane. As the Ni/Fe ratio decreases, the yield of cyclohexane first increases and then decreases. 10Ni₃-Fe₁/MCSs shows the highest yield of cyclohexane among all the catalysts (Table 3). These results imply that the addition of iron facilitates the dehydroxylation of cyclohexanol but suppresses the hydrogenation of phenol in comparison with monometallic Ni catalysts. Wang's group proved that Fe, as an oxyphilic metal, can be used to promote the selective C–O activation in m-cresol [66] and guaiacol [67] HDO on Pd-Fe catalysts. Fang et al. [40] studied the synergistic effect of bimetallic Ni-Fe catalysts on guaiacol HDO in gas-phase and suggested that the Fe species can adsorb the oxygen functionalities of guaiacol to induce the cleavage of the C–O bonds. These findings are well in accord with the results of this study, i.e. appropriate amounts of Fe significantly promote the phenol HDO process. For a comparison with bimetallic 10Ni₃-Fe₁/MCSs catalyst, a physical mixture of 10Ni/MCSs and 10Fe/MCSs catalyst was evaluated in phenol HDO. As listed in Table 3, although the conversion of phenol is more than 99%, the yield of cyclohexane (16.4%) is much lower than that of bimetallic 10Ni₃-Fe₁/MCSs catalyst (49.8%). Obviously, the physical mixture of the two monometallic catalysts lacks the synergistic effect between Ni and Fe species as bimetallic 10Ni₃-Fe₁/MCSs. The formation of Ni-Fe alloy on the latter catalyst could be the main reason for its higher selectivity to cyclohexane due to its remarkable dehydroxylation activity. In addition, a small amount of lightweight hydrocarbons resulted from the break of C–C bonds on Ni [68] are detected in gas-product (Fig. S2 and Table S2).

3.3. Reaction paths for phenol HDO on 10Ni-Fe/MCSs

Saidi et al. [2] summarized the reaction network of phenol HDO over different catalysts into two reaction paths: direct hydrogenolysis to benzene (DDO) and hydrogenation followed by dehydroxylation to cyclohexane (HYD). The reaction path of phenols HDO on bimetallic Ni-Fe catalysts should be greatly affected by H_2 pressure. The products containing benzene ring are generally obtained under lower H_2 pressure (about 1 bar), [39,69,70]. While high H_2 pressure is beneficial to the hydrogenation of benzene ring [40]. Similarly, Hsu et al. [71] investigated the HYD and DDO rates of p-cresol on NiFe catalyst at 250 °C and 10 bar H_2 pressure, finding that HYD rate was much higher than that of DDO. As shown in Table 3, the selectivity of benzene is 15.0% on 10Fe/MCSs, which is higher than the other catalysts containing metal Ni. When monometallic Ni catalyst was physically mixed with 10Fe/MCSs, the production of benzene ring saturated compounds (cyclohexane and cyclohexanol) is dominant. It should be caused by the excellent hydrogenation activity of monometallic Ni catalyst and the weaker oxophilicity of monometallic Fe-based catalyst.

To further investigate the reaction path of phenol HDO on bimetallic Ni-Fe catalysts, as one of the intermediate products of phenol HDO, the dehydroxylation of cyclohexanol was evaluated under the same reaction conditions as the HDO of phenol. As summarized in Table 4, the conversion of cyclohexanol over monometallic 10Ni/MCSs is 14.4%, and the major product is cyclohexane. However, monometallic Fe catalyst shows much lower cyclohexanol conversion (7.5%) and cyclohexane selectivity (8.9%) than those of 10Ni/MCSs, though Fe is reported to have excellent ability in C–O scission [72]. Besides, 10Fe/MCSs presents a significantly higher selectivity to cyclohexene

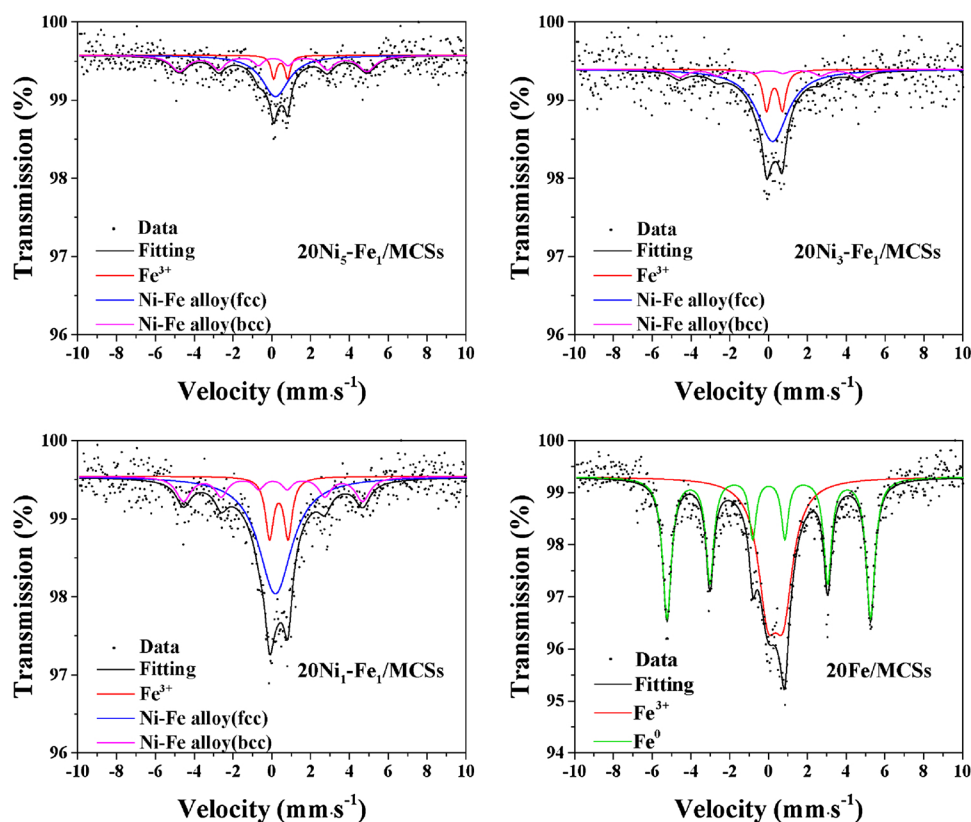


Fig. 4. Mössbauer spectra of bimetallic 20Ni-Fe/MCSs and monometallic 20Fe/MCSs.

(51.5%) than all the other catalysts. The reaction pathway of cyclohexanol dehydroxylation over monometallic Fe catalyst is similar as that of acid catalysts, on which, dehydration of cyclohexanol to cyclohexene occurs [73,74]. In this work, only a small number of acidic sites assigned to Fe^{3+} species [42,48] were detected by NH_3 -TPD method on monometallic Fe catalysts (Fig. S3), which could slightly promote the dehydration of cyclohexanol to cyclohexene. When Ni was added into Fe-based catalyst, both the conversion of cyclohexanol and the yield of cyclohexane were greatly improved and the highest performance can be achieved on the catalyst with Ni/Fe ratio of 3/1, on which the conversion and cyclohexane yield reach 57.6% and 56.6%, respectively. Therefore, not only Fe species are necessary to activate C–O bonds but also Ni species to activate hydrogen for the dehydroxylation of cyclohexanol to cyclohexane. Moreover, the selectivity to cyclohexane is higher than 95% over all the Ni-containing catalysts

regardless of the Ni content. Hence, the hydrogenolysis of cyclohexanol becomes the main reaction pathway for the dehydroxylation of cyclohexanol upon bimetallic Ni-Fe/MCSs catalysts [34,75]. In addition, excess of nickel content in the catalysts will also give rise to a dramatic decrease of the cyclohexane yield, which should be attributed to the insufficient Fe species for the activation of C–O bonds. The reaction paths for phenol HDO over bimetallic Ni-Fe catalysts are depicted in Scheme 1. Comparing the yields of cyclohexane achieved in phenol HDO with that obtained in cyclohexanol hydrogenolysis, it can be found that they display the similar volcanic trends though their initial reactants are different (Fig. S4). Hence, we deduce that the reaction rates of phenol hydrogenation should be much higher than those of cyclohexanol hydrogenolysis, leading to the accumulation of cyclohexanol. In turn, the cyclohexanol hydrogenolysis reaction rate determines the overall rate of cyclohexane formation. This is further

Table 2

Mössbauer parameters of bimetallic 20Ni-Fe/MCSs and monometallic 20Fe/MCSs.

Catalysts	IS ^a /mm·s ⁻¹	QS ^b /mm·s ⁻¹	H ₀ ^c /T	Area ^d /%	ID
20Ni ₅ -Fe ₁ /MCSs	0.46	0.72	–	10.1	Fe^{3+}
	0.19	–	–	45.9	Ni-Fe alloy (fcc)
	0.07	–	30.1	44.0	Ni-Fe alloy (bcc)
20Ni ₃ -Fe ₁ /MCSs	0.30	0.81	–	17.7	Fe^{3+}
	0.21	–	–	58.2	Ni-Fe alloy (fcc)
	0.01	–	28.7	24.1	Ni-Fe alloy (bcc)
20Ni ₁ -Fe ₁ /MCSs	0.37	0.96	–	15.5	Fe^{3+}
	0.19	–	–	61.8	Ni-Fe alloy (fcc)
	0.06	–	28.7	22.3	Ni-Fe alloy (bcc)
20Fe/MCSs	0.36	0.81	–	47.0	Fe^{3+}
	0.01	–	32.6	53.0	Fe^0

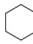
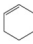

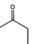
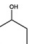
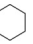
^a Isomer shift.

^b Quadrupole splitting.

^c Hyperfine magnetic field.



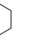

^d Relative spectral area.

Table 3Catalytic performance for phenol HDO on 10Ni/MCSs, 10Fe/MCSs and bimetallic 10Ni-Fe/MCSs catalysts.^a

Catalysts	Conv./%	Selec./%						Yield/%
								
10Ni/MCSs	99.6	8.7	0.0	1.0	2.1	88.2	8.7	
10Ni ₅ -Fe ₁ /MCSs	99.7	30.6	0.0	0.0	1.0	68.4	30.5	
10Ni ₃ -Fe ₁ /MCSs	99.8	49.9	0.0	0.0	1.0	49.1	49.8	
10Ni ₁ -Fe ₁ /MCSs	99.7	35.5	0.0	0.2	1.0	63.3	35.4	
10Ni ₁ -Fe ₃ /MCSs	82.3	34.1	0.3	0.4	1.2	64.0	28.1	
10Fe/MCSs	6.4	3.7	3.8	15.0	10.5	67.1	0.2	
10Ni/MCSs + 10Fe/MCSs	99.8	16.4	0.0	1.1	2.2	80.3	16.4	

^a Reaction conditions: P(H₂) = 5 MPa, T = 250 °C, m(catalysts) = 50 mg, m(phenol) = 0.5 g, m(n-dodecane) = 24.5 g, reaction time = 10 h, stirring speed = 800 rpm.

Table 4Catalytic performance for cyclohexanol hydrogenolysis on bimetallic 10Ni-Fe/MCSs catalysts.^a

Catalysts	Conv./%	Selec./%				Yield/%
						
10Ni/MCSs	14.4	95.8	0.0	4.2	13.8	
10Ni ₅ -Fe ₁ /MCSs	40.5	97.4	0.0	2.6	39.4	
10Ni ₃ -Fe ₁ /MCSs	57.6	98.3	0.0	1.7	56.6	
10Ni ₁ -Fe ₁ /MCSs	45.5	97.7	0.3	2.0	44.5	
10Ni ₁ -Fe ₃ /MCSs	29.4	96.0	0.9	4.0	28.2	
10Fe/MCSs	7.5	8.9	51.5	39.6	0.7	

^a Reaction conditions: P(H₂) = 5 MPa, T = 250 °C, m(catalysts) = 50 mg, m(cyclohexanol) = 0.5 g, m(n-dodecane) = 24.5 g, reaction time = 10 h, stirring speed = 800 rpm.

proved by kinetics study in Section 3.4. The detection of cyclohexanone suggests that it may be an intermediate product during phenol hydrogenation to cyclohexanol, and that the hydrogenation of cyclohexanone to cyclohexanol is much faster than the hydrogenation of phenol to cyclohexanone over the catalysts with high hydrogenation activity [9,22,73]. As consequence, the major products of phenol HDO over the bimetallic Ni-Fe/MCSs catalysts are cyclohexane and cyclohexanol, while the yields of cyclohexanone and cyclohexene are very low.

3.4. Kinetics of phenol HDO on 10Ni-Fe/MCSs

As shown in Scheme 1, hydrogenation of phenol and hydrogenolysis of cyclohexanol are important reaction steps in phenol HDO, so kinetic evaluation for these two steps were performed over 10Ni₃-Fe₁/MCSs. The conversion versus time and Arrhenius graphs for HDO of phenol and hydrogenolysis of cyclohexanol are plotted in Fig. 5. The R (reaction rates in mmol·g_{cat}⁻¹·h⁻¹) and apparent activation energy (E_a) calculation results for each step are summarized in Table 5. At different

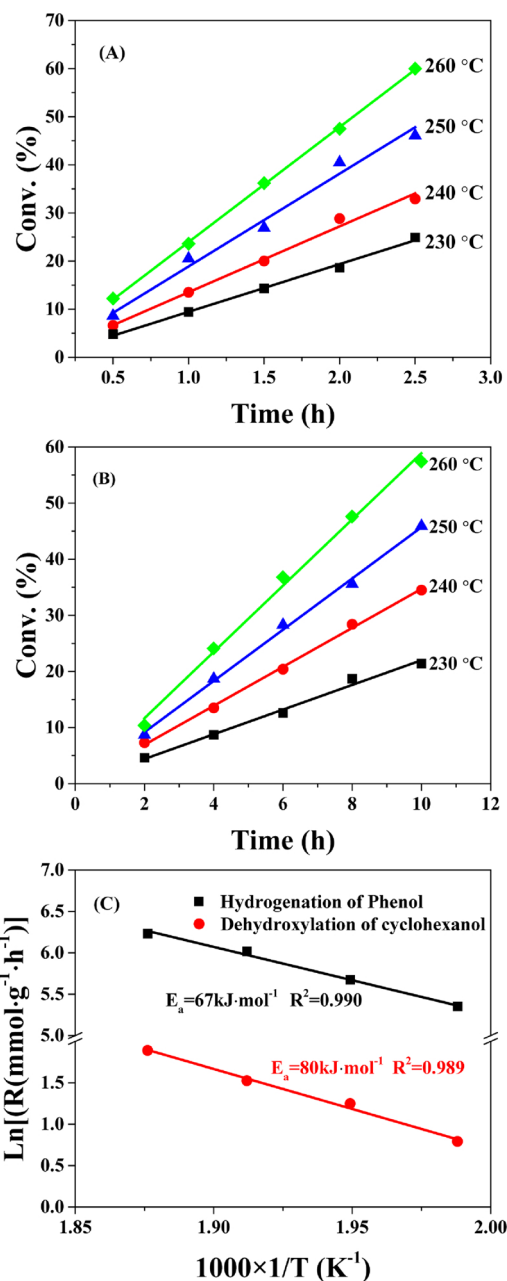
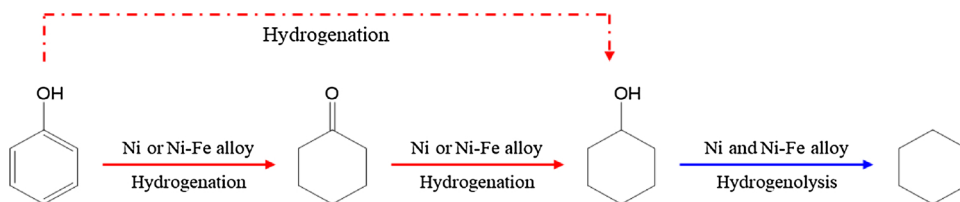


Fig. 5. (A) Conversion of phenol, (B) conversion of cyclohexanol over 10Ni₃-Fe₁/MCSs catalysts with different reaction time and temperature and (C) The R for Arrhenius plots. Reaction conditions: m(catalysts) = 20 mg, m(phenol) = 4.0 g, m(n-dodecane) = 21.0 g for the hydrogenation of phenol; m(catalysts) = 50 mg, m(cyclohexanol) = 0.5 g, m(n-dodecane) = 24.5 g for the hydrogenolysis of cyclohexanol; P(H₂) = 5 MPa and stirring speed = 800 rpm.



Scheme 1. Reaction paths for phenol HDO on bimetallic Ni-Fe catalysts. The solid arrows represent the actual reaction path, the dashed arrows represent the simplified reaction path in the kinetic model, the red arrows represent the fast reaction steps, and the blue arrows represent the rate-determining step. (For interpretation of the references to colour in this figure legend, the reader is referred to the web version of this article.)

Table 5Reaction rates and E_a values of individual steps for phenol HDO over 10Ni₃-Fe₁/MCSSs.

Steps	R/mmole _{cat} ⁻¹ h ⁻¹				E_a /kJ·mol ⁻¹
	230 °C	240 °C	250 °C	260 °C	
Hydrogenation of phenol	210.8	291.1	410.0	508.1	67
Hydrogenolysis of cyclohexanol	2.2	3.5	4.6	6.6	80

temperatures, the conversion increases linearly against reaction time for both reactions. The reaction rate of phenol hydrogenation is much higher than that of cyclohexanol hydrogenolysis by two orders of magnitude (Table 5). Moreover, the apparent activation energies for hydrogenation of phenol and hydrogenolysis of cyclohexanol are 67 and 80 kJ·mol⁻¹ on 10Ni₃-Fe₁/MCS, respectively. Hence, it is the hydrogenolysis of cyclohexanol that controls the overall reaction rate of phenol HDO. A catalyst with high activity in cyclohexanol hydrogenolysis should greatly benefit the formation of cyclohexane in phenol HDO system.

3.5. Roles of metal Ni and Ni-Fe alloy in phenol HDO

In order to reveal the reaction mechanism of phenol HDO more accurately, the bimetallic Ni-Fe catalysts with 20 wt. % of total metal loading were characterized by H₂-chemisorption and cyclohexanol uptake/withdrawal-TG. H₂ chemisorption is recognized for obtaining H₂ uptake. While for cyclohexanol, TG analysis technique was employed to examine the cyclohexanol uptake.

H₂ uptake of bimetallic 20Ni-Fe/MCSs catalysts is listed in Table S1, which has the same trend than 10Ni-Fe/MCSs (Table 1), i.e. H₂ uptake decreased sharply with the decreasing Ni/Fe ratio. Fig. 6 shows the chemisorption and desorption of cyclohexanol on bimetallic 20Ni-Fe/MCSs catalysts. The cyclohexanol uptake on the catalysts increases from 129 mol·g_{cat}⁻¹ to 187 μmol·g_{cat}⁻¹ with decreasing Ni/Fe ratio (Fig. 6A). This suggests that the amounts of active sites for the chemisorption of cyclohexanol are improved significantly on account of the increasement of Fe content. To identify the strength of the active sites in adsorbing cyclohexanol, the cyclohexanol desorption rate was characterized by DTG analysis. According to Fig. 6B, compared with the desorption temperature of cyclohexanol (360 °C) for 20Ni₅-Fe₁/MCSs catalyst, 20Ni₃-Fe₁/MCSs catalyst exhibits a higher desorption temperature of 370 °C. However, for 20Ni₁-Fe₁/MCSs and 20Ni₁-Fe₃/MCSs catalysts, no such a desorption temperature peak is found, indicating that the adsorbed cyclohexanol cannot desorb by these catalysts at temperature below 400 °C due to the strong chemisorption ability (Further improving desorption temperature is meaningless since the catalyst was

only pretreated at 400 °C in N₂). That is to say, the interaction between cyclohexanol and the active sites is gradually enhanced as Ni/Fe ratio decreasing.

The catalytic performances of the 20Ni-Fe/MCSs in phenol HDO and cyclohexanol are summarized in Table S3 and Table S4. As expected, with Ni/Fe ratio decreasing, the catalysts with a loading of 20 wt.% presented the same variation trend of catalytic performance as the catalysts with a loading of 10 wt.%. In bimetallic catalysts, Ni-Fe alloy could be easily generated at the interface between Ni and Fe nanoparticles. As is well known, the hydrogen activated by metal Ni sites can only overflow to the adjacent and closely contacted Ni-Fe alloy sites for the hydrogenation. For synergetic role, according to the results of H₂ uptake normalized by the mass of nickel (Table S1), it can be found that the addition of iron inhibits the H₂ adsorption on nickel. The surface segregation of iron species on the Ni nanoparticles led to the formation of Ni-Fe alloy at the interface, which is not conducive to the adsorption of H₂ on the catalyst. Therefore, it indicates that H₂ can be more easily chemisorbed on metal Ni sites than Ni-Fe alloy. Meanwhile, the results of Mössbauer spectra (Table 2) show that there are only two kinds of iron phases on Ni-Fe bimetallic catalysts: Fe³⁺ and Ni-Fe alloy. Obviously, Fe³⁺ cannot be the active sites for the conversion of cyclohexanol, which has been proved by the evaluation of Fe/MCSs in cyclohexanol hydrogenolysis (Table 4). Thus, it can be speculated that the adsorption of cyclohexanol is mainly attributed to Ni-Fe alloy active sites. Therefore, in terms of main active sites for the adsorption of H₂ and cyclohexanol, the activation of hydrogen should occur primarily on metal Ni sites, while the adsorption and cleavage of C–O bonds are mainly dependent on Ni-Fe alloy active sites for phenol HDO on the Ni-Fe/MCSs catalysts.

In a bifunctional catalyst system, the correlation between the turnover frequency (TOF) of one kind of active site with the amounts of the other is a common method for discussing their synergy [76–78]. To correlate the two kinds of active sites with the catalytic activity in the hydrogenolysis of cyclohexanol, TOF values of both Ni and Ni-Fe alloy were calculated. H₂ uptake was considered as the amount of metal Ni sites, and the cyclohexanol uptake was regarded as the amount of Ni-Fe alloy active sites. As plotted in Fig. 7A, the TOF_{Ni} increases linearly with increasing the amount of Ni-Fe alloy active sites, which is a powerful evidence for the beneficial effect of Ni-Fe alloy sites on improving the utilization of metal Ni sites. Differently, the TOF_{Ni-Fe} exhibits a maximum value with the increasing of metal Ni sites (Fig. 7B). It seems that too high H₂ coverage does not benefit the activation of cyclohexanol, leading to a decrease of TOF_{Ni-Fe}. The excess metal Ni active sites can provide too much dissociated H, which could spill over to the nearby Ni-Fe alloy sites, inhibiting the cyclohexanol adsorption. Musci et al. [79] found that the moderate addition of Sn could promote the C = O hydrogenation, and a higher Sn content will result in dilution

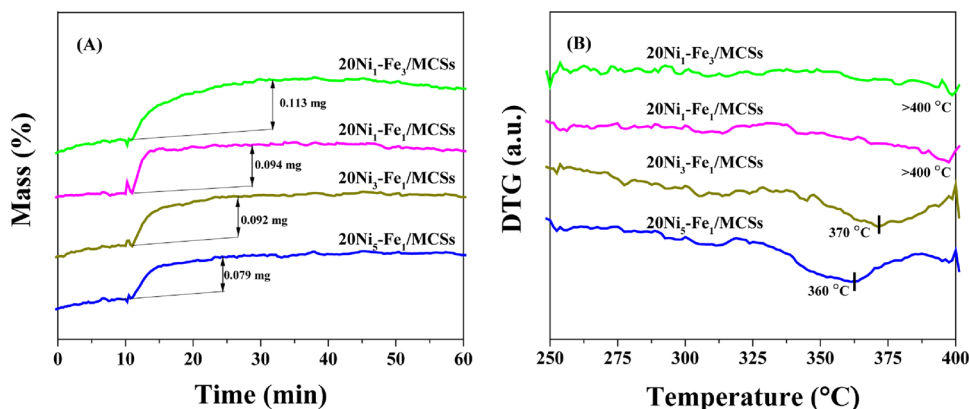


Fig. 6. (A) TG analysis curves for cyclohexanol chemisorption and (B) DTG analysis curves for cyclohexanol desorption over bimetallic 20Ni-Fe/MCSs catalysts with varying Ni/Fe ratios.

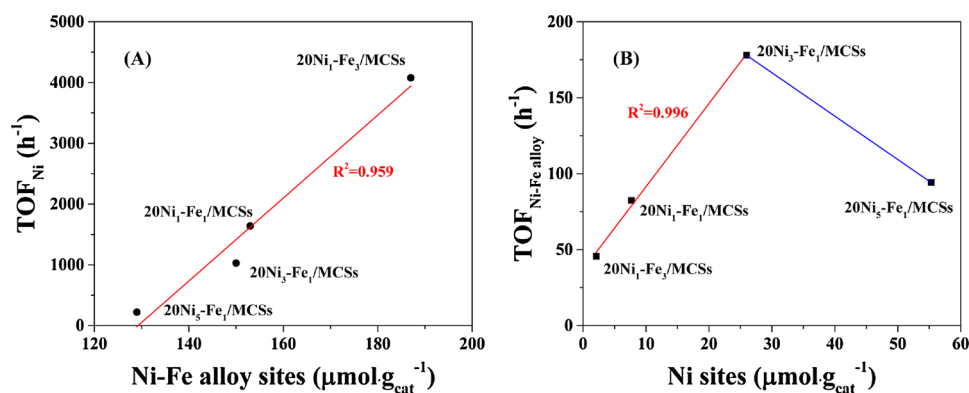
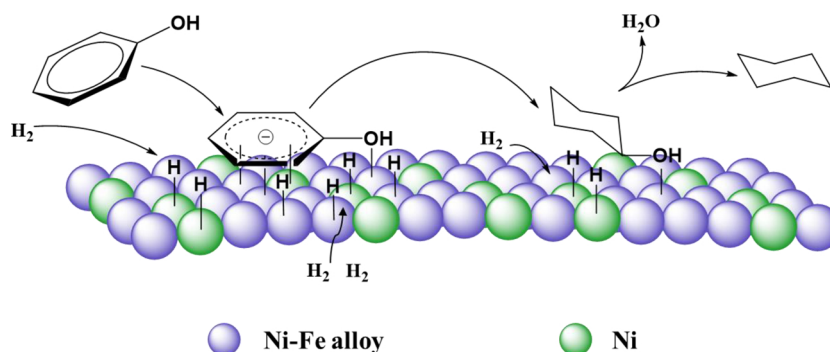


Fig. 7. Effects of (A) Ni-Fe alloy sites for cyclohexanol and (B) metallic Ni sites for H₂ on the catalytic performance of bimetallic Ni-Fe/MCSs catalysts for the hydrogenolysis of cyclohexanol.



Scheme 2. Proposed reaction mechanism for phenol HDO on the surface of bimetallic Ni-Fe catalysts.

of Ru sites on bimetallic RuSn catalysts in furfural hydrogenation. Wang et al. [80] demonstrated by density functional theory method that the barrier for hydrogenation and decarbonylation of furfural over Pd (111) could reach the lowest value under intermediate degree of H coverage. To sum up, there is a synergistic effect between metal Ni and Ni-Fe alloy sites in bimetallic Ni-Fe catalysts, which facilitates the hydrogenolysis of cyclohexanol to cyclohexane, as well as the phenol HDO.

On basis of above results, a reaction mechanism for phenol HDO over bimetallic Ni-Fe catalysts is proposed as shown in Scheme 2. To simplify the catalyst model, metal Ni sites and Ni-Fe alloy sites are represented as single spheres. The aromatic ring of phenol can be adsorbed parallelly on the surface of metal Ni or Ni-Fe alloy [81], and the oxygen functional group of phenol is mainly adsorbed on Ni-Fe alloy sites [82,83]. Then, the adsorbed aromatic ring can react easily with the dissociated hydrogen by metallic Ni sites to form cyclohexanol. Similarly, Ni-Fe alloy sites favor the adsorption of cyclohexanol via the hydroxy group, followed by the hydrogenolysis of cyclohexanol to generate cyclohexane.

In addition, both the cyclohexanol conversion and TOF_{Ni-Fe} of 20Ni₃-Fe₁/MCSs are the highest among the suite of bimetallic Ni-Fe catalysts in the hydrogenolysis of cyclohexanol. Except for the explanation mentioned above that the excessive adsorption of hydrogen on the active sites are not conducive to the adsorption of cyclohexanol, the adsorption strength between cyclohexanol with Ni-Fe alloy sites might also affect the activity of the catalysts. Appropriate adsorption strength of cyclohexanol on active sites could promote the activity of the catalyst, while the excessive strong adsorption of cyclohexanol may result in the severe trapping of cyclohexanol on the catalyst surface, which is not conducive to the conversion of cyclohexanol [84].

3.6. HDO of other lignin-derived phenols

There are many kinds of lignin-derived phenolic compounds during

Table 6

Catalytic performance for the HDO of other lignin-derived phenols on 20Ni₃-Fe₁/MCSs.^a

Compounds	Structural formula	Conv./%	Main product	Select./%	
				Oxygen-containing	Hydrocarbons
Catechol		99.9		29.6	70.4
Guaiacol		99.4		6.1	93.9
p-Cresol		99.9		3.3	96.7
Eugenol		99.9		5.5	94.5

^a Reaction conditions: P(H₂) = 5 MPa, T = 250 °C, m(catalysts) = 50 mg, m(phenols) = 0.5 g, m(n-dodecane) = 24.5 g, reaction time = 10 h, stirring speed = 800 rpm.

the degradation of lignin, such as catechol, guaiacol, cresol, eugenol and so on. Here, the hydrodeoxygenation of these phenols was also conducted on the 20Ni₃-Fe₁/MCSs bimetallic catalyst. As listed in Table 6, the conversion of all tested phenols is close to 100%, and the main products are all cyclohexane/alkyl cyclohexane. The selectivity to hydrocarbons for catechol HDO (70%) is much lower than those of other phenols (~95%). This should be attributed to the presence of two hydroxyl groups in each catechol molecule, whose hydrogenolysis certainly requires longer interactions with the catalyst. The guaiacol and eugenol can be demethoxylated. Taking guaiacol as an example, if the methoxy functional group is demethylated, it will be converted into catechol, which can be further hydrodeoxygenated to hydrocarbon. However, as shown in Table 6, the hydrocarbon selectivity obtained in catechol HDO (70.4%) is much lower than that in guaiacol HDO (93.9%), indicating that the deoxygenation rate of catechol is lower

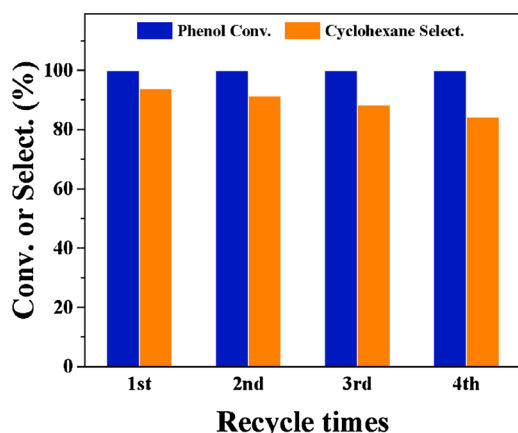


Fig. 8. Stability of 20Ni₃Fe₁/MCSs for phenol HDO. Reaction conditions: P (H₂) = 5 MPa, T = 250 °C, m(20Ni₃Fe₁/MCSs) = 50 mg, m(phenol) = 0.5 g, m (n-dodecane) = 24.5 g, reaction time = 10 h, stirring speed = 800 rpm.

than that of guaiacol. It means that the methoxyl group of guaiacol and eugenol should be mainly eliminated by direct demethoxylation instead of demethylation. It is worth mentioning that the side alkyl chain of eugenol does not break despite of the presence of highly active Ni sites, which is advantage for selective HDO of lignocellulosic bio-oil. The outstanding catalytic performance and the universality of 20Ni₃-Fe₁/MCSs catalyst provide an inspiration for the development of highly efficient catalyst for the HDO of lignin-derived phenols.

3.7 Stability of 20Ni₃Fe₁/MCSs for phenol HDO

The reusability of 20Ni₃Fe₁/MCSs with the best performance among this series of 20Ni-Fe/MCSs catalysts is shown in Fig. 8. A slight decline in cyclohexane selectivity was found during 4 recycles evaluation (average decrease is about 2.5% for each 10-hour evaluation). The decrease in cyclohexane selectivity might be ascribed to not only the minor deactivation of the catalyst but also the small catalyst loss during the recycle process. However, this minor deactivation should not affect the variation trend of the apparent activity for various catalysts, as well as the conclusions made in this work. Further improvement on the stability of bimetallic Ni-Fe catalysts would be necessary.

4. Conclusions

A suite of novel Ni-Fe bimetallic nanoparticles supported on MCSs with varying Ni/Fe ratios have been applied in the production of cyclohexane via liquid-phase hydrodeoxygenation of phenol. Owing to the formation of Ni-Fe alloy, bimetallic Ni-Fe catalysts exhibited better performance in the yield of cyclohexane than the monometallic catalysts. Among these bimetallic Ni-Fe catalysts, 20Ni₃-Fe₁/MCSs with Ni/Fe ratio of 3/1 presented the highest cyclohexane yield of 93.8%. The apparent activation energies for hydrogenation of phenol and hydrogenolysis of cyclohexanol over Ni₃-Fe₁/MCSs were found to be 67 and 80 kJ·mol⁻¹, respectively. The large differences between the reaction rates of phenol and cyclohexanol (410.0 versus 4.6 mmol·g_{cat}⁻¹ h⁻¹) indicate that the hydrogenolysis of cyclohexanol is the rate-determining step for phenol HDO. It was also demonstrated that the synergy between the metallic Ni sites and Ni-Fe alloy active sites enables H₂ activation and the cleavage of C–O bonds facilitating the HDO of phenolic compounds all the way to cycloalkanes. The presence of more active sites for cyclohexanol adsorption on Ni-Fe/MCSs than on monometallic counterparts significantly improves the catalytic performance. These findings provide guidance for new strategies in the rational design of catalysts for HDO of phenolic compounds.

Acknowledgements

We are grateful to the financial support from the National Natural

Science Foundation of China (21878227, U1510203). O.Y.G. and J.A.L. were supported by the U.S. Department of Energy (DOE), Office of Basic Energy Sciences (BES), Division of Chemical Sciences, Geosciences and Biosciences.

Appendix A. Supplementary data

Supplementary material related to this article can be found, in the online version, at doi:<https://doi.org/10.1016/j.apcatb.2019.04.065>.

References

- [1] Q. Bu, H. Lei, A.H. Zacher, L. Wang, S. Ren, J. Liang, Y. Wei, Y. Liu, J. Tang, Q. Zhang, R. Ruan, *Bioresour. Technol.* 124 (2012) 470–477.
- [2] M. Saidi, F. Samimi, D. Karimipourfard, T. Nimmanwudipong, B.C. Gates, *Energy Environ. Sci.* 7 (2014) 103–129.
- [3] X. Li, G. Chen, C. Liu, W. Ma, B. Yan, J. Zhang, *Renew. Sust. Energy Rev.* 71 (2017) 296–308.
- [4] S. Czernik, A.V. Bridgwater, *Energy Fuels* 18 (2004) 590–598.
- [5] C. Lindfors, E. Kuoppala, A. Oasmaa, Y. Solantausta, V. Arpiainen, *Energy Fuels* 28 (2014) 5785–5791.
- [6] E. Furimsky, *Appl. Catal. A Gen.* 199 (2000) 147–190.
- [7] G.W. Huber, S. Iborra, A. Corma, *Chem. Rev.* 106 (2006) 4044–4098.
- [8] D. Mohan, C.U. Pittman, P.H. Steele, *Energy Fuels* 20 (2006) 848–889.
- [9] P.M. Mortensen, J. Grunwaldt, P.A. Jensen, A.D. Jensen, *ACS Catal.* 3 (2013) 1774–1785.
- [10] C. Liu, H. Wang, A.M. Karim, J. Sun, Y. Wang, *Chem. Soc. Rev.* 43 (2014) 7594–7623.
- [11] H. Wang, J. Male, Y. Wang, *ACS Catal.* 3 (2013) 1047–1070.
- [12] H. Li, A. Riisager, S. Saravanamurugan, A. Pandey, R.S. Sangwan, S. Yang, R. Luque, *ACS Catal.* 8 (2017) 148–187.
- [13] Y. Hong, A. Hensley, J. McEwen, Y. Wang, *Catal. Lett.* 146 (2016) 1621–1633.
- [14] V. Ithibenchapong, C. Ratanatawanate, M. Oura, K. Faungnawakij, *Catal. Commun.* 68 (2015) 31–35.
- [15] B. Yoosuk, D. Tumnantong, P. Prasassarakich, *Chem. Eng. Sci.* 79 (2012) 1–7.
- [16] E. Ryymin, M.L. Honkela, T. Viljava, A.O.I. Krause, *Appl. Catal. A Gen.* 389 (2010) 114–121.
- [17] P.M. Mortensen, D. Gardini, C.D. Damsgaard, J. Grunwaldt, P.A. Jensen, J.B. Wagner, A.D. Jensen, *Appl. Catal. A Gen.* 523 (2016) 159–170.
- [18] P. Dufresne, *Appl. Catal. A Gen.* 322 (2007) 67–75.
- [19] X. Zhu, L.L. Lobban, R.G. Mallinson, D.E. Resasco, *J. Catal.* 281 (2011) 21–29.
- [20] C. Zhao, W. Song, J.A. Lercher, *ACS Catal.* 2 (2012) 2714–2723.
- [21] H. Ohta, K. Yamamoto, M. Hayashi, G. Hamasaka, Y. Uozumi, Y. Watanabe, *Chem. Commun. (Camb.)* 51 (2015) 17000–17003.
- [22] P.M. de Souza, R.C. Rabelo-Neto, L.E.P. Borges, G. Jacobs, B.H. Davis, T. Sooknoi, D.E. Resasco, F.B. Noronha, *ACS Catal.* 5 (2015) 1318–1329.
- [23] M. Lu, H. Du, B. Wei, J. Zhu, M. Li, Y. Shan, J. Shen, C. Song, *Ind. Eng. Chem. Res.* 56 (2017) 12070–12079.
- [24] C. Zhao, J. He, A.A. Lemonidou, X. Li, J.A. Lercher, *J. Catal.* 280 (2011) 8–16.
- [25] A.M. Robinson, J.E. Hensley, J.W. Medlin, *ACS Catal.* 6 (2016) 5026–5043.
- [26] H. Ren, W. Yu, M. Saliccioli, Y. Chen, Y. Huang, K. Xiong, D.G. Vlachos, J.G. Chen, *Chemsuschem* 6 (2013) 798–801.
- [27] P.M. Mortensen, H.W.P. de Carvalho, J. Grunwaldt, P.A. Jensen, A.D. Jensen, *J. Catal.* 328 (2015) 208–215.
- [28] H.Y. Zhao, D. Li, P. Bui, S.T. Oyama, *Appl. Catal. A-Gen.* 391 (2011) 305–310.
- [29] Y. Bonita, J.C. Hicks, *J. Phys. Chem. C* 25 (2018) 13322–13332.
- [30] D.A. Ruddy, J.A. Schaidle, J.R. Ferrell, J. Wang, L. Moens, J.E. Hensley, *Green Chem.* 16 (2014) 454–490.
- [31] S. Oh, H.S. Choi, I. Choi, J.W. Choi, *RSC Adv.* 7 (2017) 15116–15126.
- [32] X. Liu, W. Jia, G. Xu, Y. Zhang, Y. Fu, *ACS Sustain. Chem. Eng.* 5 (2017) 8594–8601.
- [33] R.N. Olcese, M. Bettahar, D. Petitjean, B. Malaman, F. Giovannella, A. Dufour, *Appl. Catal. B Environ.* 115–116 (2012) 63–73.
- [34] S. Echeandia, P.L. Arias, V.L. Barrio, B. Pawelec, J.L.G. Fierro, *Appl. Catal. B Environ.* 101 (2010) 1–12.
- [35] A. Robinson, G.A. Ferguson, J.R. Gallagher, S. Cheah, G.T. Beckham, J.A. Schaidle, J.E. Hensley, J.W. Medlin, *ACS Catal.* 6 (2016) 4356–4368.
- [36] S. Jin, Z. Xiao, C. Li, X. Chen, L. Wang, J. Xing, W. Li, C. Liang, *Catal. Today* 234 (2014) 125–132.
- [37] S. Sathisa, W. An, D.E. Resasco, *J. Catal.* 284 (2011) 90–101.
- [38] X. Yu, J. Chen, T. Ren, *RSC Adv.* 4 (2014) 46427–46436.
- [39] L. Nie, P.M. de Souza, F.B. Noronha, W. An, T. Sooknoi, D.E. Resasco, *J. Mol. Catal. A Chem.* 388–389 (2014) 47–55.
- [40] H. Fang, J. Zheng, X. Luo, J. Du, A. Roldan, S. Leoni, Y. Yuan, *Appl. Catal. A Gen.* 529 (2017) 20–31.
- [41] J. Wang, Q. Chen, X. Liu, W. Qiao, D. Long, L. Ling, *Mater. Chem. Phys.* 129 (2011) 1035–1041.
- [42] C. Li, G. Xu, Y. Zhai, X. Liu, Y. Ma, Y. Zhang, *Fuel* 203 (2017) 23–31.
- [43] D. Li, M. Koike, L. Wang, Y. Nakagawa, Y. Xu, K. Tomishige, *Chemsuschem* 7 (2014) 510–522.
- [44] Z. Zheng, C. Sun, R. Dai, S. Wang, X. Wu, X. An, Z. Wu, X. Xie, *Energy Fuels* 31 (2017) 3091–3100.
- [45] B.D. Chandler, A.B. Schabel, L.H. Pignolet, *J. Phys. Chem. B* 105 (2001) 149–155.

- [46] H. Yen, Y. Seo, S. Kaliaguine, F. Kleitz, *ACS Catal.* 5 (2015) 5505–5511.
- [47] P. Jing, M. Liu, Y. Pu, Y. Cui, Z. Wang, J. Wang, Q. Liu, *Sci. Rep.* 6 (2016).
- [48] Y. Zhai, C. Li, G. Xu, Y. Ma, X. Liu, Z. Ying, *Green Chem.* 19 (2017) 1859–1903.
- [49] W. Gao, C. Li, H. Chen, M. Wu, S. He, M. Wei, D.G. Evans, X. Duan, *Green Chem.* 16 (2014) 1560.
- [50] V. Ospina, R. Buitrago, D.P. Lopez, *Eng. Invest.* 35 (2015) 49–55.
- [51] A. Nieto-Márquez, S. Gil, A. Romero, J.L. Valverde, S. Gómez-Quero, M.A. Keane, *Appl. Catal. A Gen.* 363 (2009) 188–198.
- [52] H. Li, D. Yu, Y. Hu, P. Sun, J. Xia, H. Huang, *Carbon* 48 (2010) 4547–4555.
- [53] K. Fabricovicova, O. Malter, M. Lucas, P. Claus, *Green Chem.* 16 (2014) 3580–3588.
- [54] W.K. Jozwiak, E. Kaczmarek, T.P. Maniecki, W. Ignaczak, W. Maniukiewicz, *Appl. Catal. A Gen.* 326 (2007) 17–27.
- [55] J. Zieliński, I. Zglinicka, L. Znak, Z. Kaszkur, *Appl. Catal. A Gen.* 381 (2010) 191–196.
- [56] L. Zhou, L.R. Enakonda, M. Harb, Y. Saih, A. Aguilar-Tapia, S. Ould-Chikh, J. Hazemann, J. Li, N. Wei, D. Gary, P. Del-Gallo, J. Basset, *Appl. Catal. B Environ.* 208 (2017) 44–59.
- [57] L.R. Winter, E. Gomez, B. Yan, S. Yao, J.G. Chen, *Appl. Catal. B Environ.* 244 (2018) 442–450.
- [58] L. Wang, D. Li, M. Koike, S. Koso, Y. Nakagawa, Y. Xu, K. Tomishige, *Appl. Catal. A Gen.* 392 (2011) 248–255.
- [59] T. Mizushima, K. Tohji, Y. Udagawa, M. Harada, M. Ishikawa, A. Ueno, *J. Catal.* 112 (1988) 282–289.
- [60] T. Kawabata, N. Fujisaki, T. Shishido, K. Nomura, T. Sano, K. Takehira, *J. Mol. Catal. A Chem.* 253 (2006) 279–289.
- [61] A.S. Lileev, Y.D. Yagodka, M. Reissner, W. Steiner, *J. Magn. Magn. Mater.* 258–259 (2003) 504–506.
- [62] W. Shen, Y. Wang, X. Shi, N. Shah, F. Huggins, S. Bollineni, M. Seehra, G. Huffman, *Energy Fuels* 21 (2007) 3520–3529.
- [63] W. Song, Y. Liu, E. Baráth, C. Zhao, J.A. Lercher, *Green Chem.* 17 (2015) 1204–1218.
- [64] R. Shu, Q. Zhang, Y. Xu, J. Long, L. Ma, T. Wang, P. Chen, Q. Wu, *RSC Adv.* 6 (2016) 5214–5222.
- [65] R. Shu, Y. Xu, P. Chen, L. Ma, Q. Zhang, L. Zhou, C. Wang, *Energy Fuels* 31 (2017) 7208–7213.
- [66] J. Sun, A.M. Karim, H. Zhang, L. Kovarik, X.S. Li, A.J. Hensley, J. McEwen, Y. Wang, *J. Catal.* 306 (2013) 47–57.
- [67] Y. Hong, H. Zhang, J. Sun, K.M. Ayman, A.J.R. Hensley, M. Gu, M.H. Engelhard, J. McEwen, Y. Wang, *ACS Catal.* 4 (2014) 3335–3345.
- [68] J. Chen, H. Shi, L. Li, K. Li, *Appl. Catal. B Environ.* 144 (2014) 870–884.
- [69] X. Xu, E. Jiang, Y. Du, B. Li, *Renew. Energy* 96 (2016) 458–468.
- [70] X.W. Xu, E.C. Jiang, *Energy Fuels* 31 (2017) 2855–2864.
- [71] P. Hsu, J. Jiang, Y. Lin, *ACS Sustain. Chem. Eng.* 6 (2017) 660–667.
- [72] W.H. Hung, S.L. Bernasek, *Surf. Sci.* 346 (1996) 165–188.
- [73] C. Zhao, Y. Kou, A.A. Lemonidou, X.B. Li, J.A. Lercher, *Angew. Chem. Int. Ed.* 48 (2009) 3987–3990.
- [74] C. Zhao, J.A. Lercher, *Angew. Chem. Int. Ed.* 51 (2012) 5935–5940.
- [75] S. De, J.G. Zhang, R. Luque, N. Yan, *Energy Environ. Sci.* 9 (2016) 3314–3347.
- [76] Y. Wang, Y.L. Shen, Y.J. Zhao, J. Lv, S.P. Wang, X.B. Ma, *ACS Catal.* 5 (2015) 6200–6208.
- [77] Y. Wang, Y.J. Zhao, J. Lv, X.B. Ma, *Chemcatchem* 9 (2017) 2085–2090.
- [78] Y.J. Zhao, B. Shan, Y. Wang, J.H. Zhou, S.P. Wang, X.B. Ma, *Ind. Eng. Chem. Res.* 57 (2018) 4526–4534.
- [79] J.J. Musci, A.B. Merlo, M.L. Casella, *Catal. Today* 296 (2017) 43–50.
- [80] S.G. Wang, V. Votronikov, D.G. Vlachos, *ACS Catal.* 5 (2014) 104–112.
- [81] L.D. Site, A. Alavi, C.F. Abrams, *Phys. Rev. B* 67 (2003) 193401–193406.
- [82] A.J.R. Hensley, Y. Wang, J. McEwen, *Surf. Sci.* 630 (2014) 244–253.
- [83] X.Y. Liu, W. An, C.H. Turner, D.E. Resasco, *J. Catal.* 359 (2018) 272–286.
- [84] P. Sirous-Rezaei, J. Jae, J. Ha, C.H. Ko, J.M. Kim, J. Jeon, Y. Park, *Green Chem.* 20 (2018) 1472–1483.